Journal of Marine Systems 79 (2010) 144–156

Contents lists available at ScienceDirect

Journal of Marine Systems

journal homepage: www.elsevier.com/locate/jmarsys

Sequential data assimilation applied to a physical–biological model for the Bermuda Atlantic time series station

Jann Paul Mattern [a], Mike Dowd [b,*], Katja Fennel [a]

[a] Department of Oceanography, Dalhousie University, Halifax, Nova Scotia, Canada
[b] Department of Mathematics and Statistics, Dalhousie University, Halifax, Nova Scotia, Canada

ARTICLE INFO

Article history:
Received 11 December 2008
Received in revised form 12 June 2009
Accepted 3 August 2009
Available online 12 September 2009

Keywords:
Data assimilation
Ensemble Kalman filter
Sequential importance resampling
Ecosystem model
1D ocean model
Bermuda Atlantic Time Series study
General Ocean Turbulence Model

ABSTRACT

In this study, we investigate sequential data assimilation approaches for state estimation and prediction in a coupled physical–biological model for the Bermuda Atlantic Time Series (BATS) site. The model is 1-dimensional (vertical) in space and based on the General Ocean Turbulence Model (GOTM). Coupled to GOTM is a biological model that includes phytoplankton, detritus, dissolved inorganic nitrogen, chlorophyll and oxygen. We performed model ensemble runs by introducing variations in the biological parameters, each of which was assigned a probability distribution. We compare and contrast here 2 sequential data assimilation methods: the ensemble Kalman filter (EnKF) and sequential importance resampling (SIR). We assimilated different types of BATS observations, including particulate organic nitrogen, nitrate + nitrite, chlorophyll *a* and oxygen for the 2-year period from January 1990 to December 1991, and quantified the impact of the data assimilation on the model's predictive skill. By applying a cross-validation to the data-assimilative and deterministic simulations we found that the predictive skill was improved for 2-week forecasts. In our experiments the EnKF, which exhibited a stronger effect on the ensemble during the assimilation step, showed slightly higher improvements in the predictive skill than the SIR, which preserves dynamical model consistency in our implementation. Our numerical experiments show that statistical properties stabilize for ensemble sizes of 20 or greater with little improvement for larger ensembles.

1. Introduction

Ecological and biogeochemical descriptions of the oceans' state rely increasingly on a combination of numerical ocean models and available observations through data assimilation in order to achieve realistic simulations and improved forecast abilities (Doney et al., 2001). Ecological and biogeochemical models with varying levels of complexity and coupled to realistic ocean circulation models are under active development (McGillicuddy et al., 2003; Kantha, 2004; Fennel et al., 2006; Rothstein et al., 2006; Wiggert et al., 2006; Kishi et al., 2007; Fennel et al., 2008). While new types of interdisciplinary observations from autonomous sensors are becoming available, the models still rely largely on traditional time-series and satellite data for calibration and validation. Given both, the partial observability of the system and the inherent uncertainty in the model formulations, the development of efficient and effective data assimilation approaches is important for progress in ecological and biogeochemical prediction (Hofmann and Friedrichs, 2001; Bertino et al., 2003; Arhonditsis and Brett, 2004).

Two general types of biological data assimilation have been used: variational and sequential methods. Variational approaches as applied to biological models have mostly focused on parameter optimization where model parameters are calibrated by minimizing the model's misfit against available data, and for the purpose of assessing different model configurations (Lawson et al., 1996; Fennel et al., 2001; Friedrichs, 2001; Friedrichs et al., 2007; Schartau et al., 2001; Spitz et al., 2001). Such calibrated models can form the basis for sequential data assimilation. Sequential data assimilation focuses on predictive online state estimation, i.e. an alteration of the model's state, taking into account the available observations as the model is being integrated forward in time (Bertino et al., 2003). A popular sequential approach in oceanography and meteorology is the ensemble Kalman filter (EnKF; Evensen, 2003, 2006). It has been employed successfully for biological ocean models (Allen et al., 2003; Evensen, 2003; Natvik and Evensen, 2003; Lenartz et al., 2007). A lesser-used alternative is Sequential Importance Resampling (SIR), which is well established in the fields of statistics and engineering (Gordon et al., 1993; Kitagawa, 1996; Ristic et al., 2004). SIR has been investigated in the context of biological ocean modelling using only simple box models (Losa et al., 2003; Dowd, 2007).

In this study, we investigate the use of the EnKF and SIR for biological data assimilation using observations from the Bermuda Atlantic Time Series (BATS) site (Steinberg et al., 2001). Our dynamic model is 1-dimensional (1D; depth-resolved) in space, uses the General Ocean Turbulence Model (GOTM, Burchard et al., 1999, www.

* Corresponding author.
E-mail address: mdowd@mathstat.dal.ca (M. Dowd).

0924-7963/$ – see front matter © 2009 Elsevier B.V. All rights reserved.
doi:10.1016/j.jmarsys.2009.08.004

Table 1
Biological model variables.

Name	Unit	Description
Phy	mmol N m^{-3}	Phytoplankton concentration
Det	mmol N m^{-3}	Detritus concentration
DIN	mmol N m^{-3}	Concentration of dissolved inorganic nitrogen
Chl	mg chlorophyll *a* m^{-3}	Chlorophyll a concentration
Oxy	mmol O m^{-3}	Oxygen concentration

gotm.net) as its physical framework, and is coupled to a set of biological equations based on Fennel et al. (2006).

The objectives of our study are an application of the 2 sequential ensemble assimilation methods (EnKF and SIR) to our system, and a comparative assessment of their potential use for state estimation in operational ocean prediction. Our paper is organized as follows: in Section 2 we introduce our coupled physical–biological model and our approach to ensemble generation based on stochastic parameters; in Section 3 we briefly review the EnKF and SIR and their application. We report results of our simulations and data assimilation experiments in Section 4, and discuss our main findings in Section 5.

2. Model description

Our physical–biological model uses a relatively simple representation of euphotic zone nitrogen cycling coupled with a 1D physical model of the upper ocean. It is implemented for the BATS site at 30°40'N, 64°10'W in the Sargasso Sea. The biological module includes the following 5 state variables: dissolved inorganic nitrogen, phytoplankton biomass and chlorophyll, detritus, and oxygen (Table 1), and is described in more detail below. Our physical model is GOTM (Burchard et al., 1999), which we implemented for the top 350 m with a vertical resolution of 1 m. We use the k-epsilon mixing scheme (Rodi, 1987) and force the model with daily wind stresses, air temperatures, air pressures, and relative humidity values from the NCEP reanalysis data set (Kalnay et al., 1996, www.noaa.gov). Nitrate is clamped to its climatological mean concentrations at 350 m depth, all other biological variables are not constrained at the bottom. Sinking organic matter leaves the model domain upon reaching the bottom boundary.

The BATS site is characterized by the frequent passage of mesoscale eddies, which are known to influence the biological dynamics through vertical displacements of isopycnals but are not resolved in our 1D model. In order to capture the influence of shoaling and deepening isopycnals on the mixed layer depth, we nudge model temperatures and salinities to their corresponding observed profiles. Without nudging, the model significantly underestimates observed mixed layer depths, which we calculated as the depth at which the water temperature first drops 0.5 °C below the surface temperature. We found that a nudging time scale of 7 days results in a close agreement between model-simulated and observed values of mixed layer depth (Fig. 1) with a coefficient of determination (R^2) of 86% compared to 52% for a nudging time scale of 1 month.

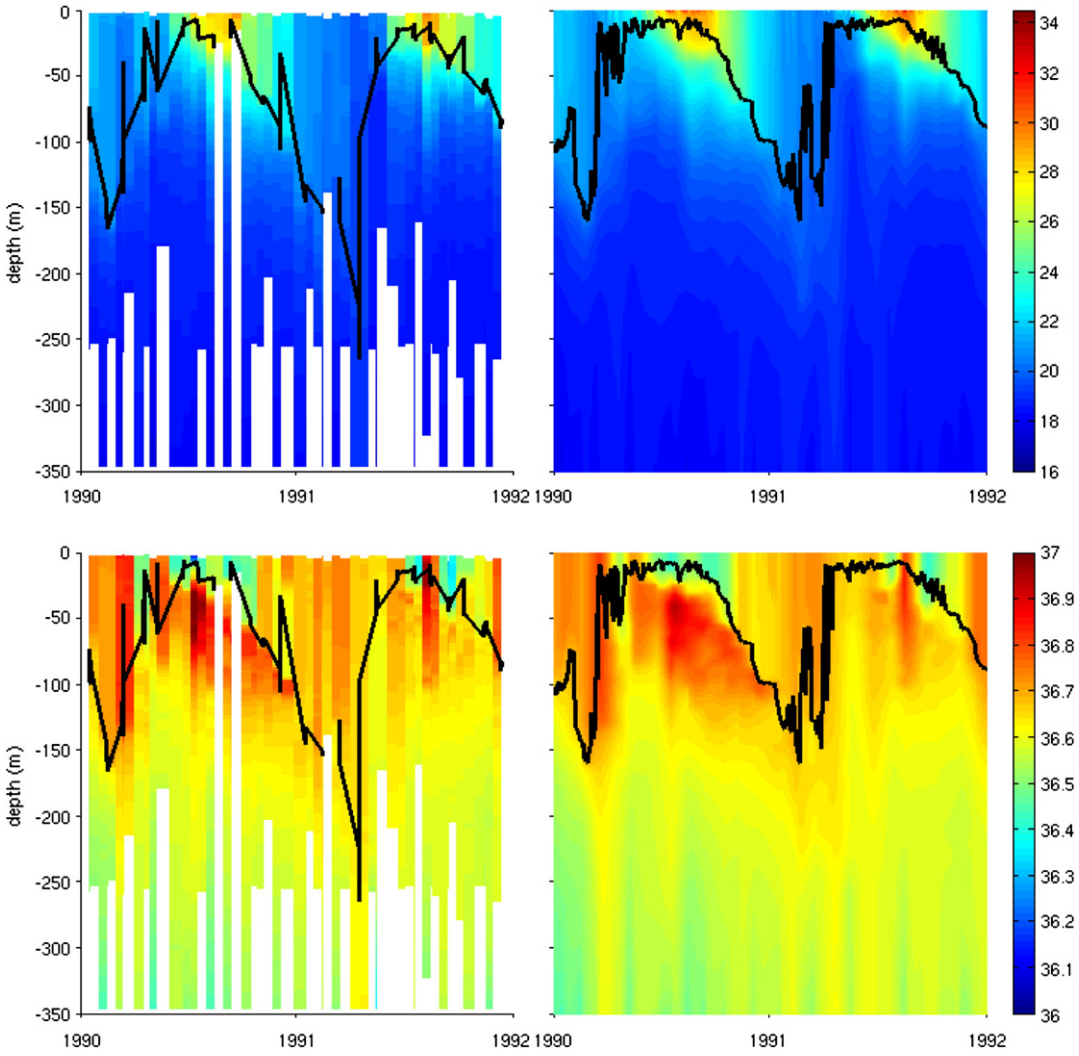

Fig. 1. Observed and model-simulated temperature (top panels, left and right respectively) and salinity (bottom panels) as well as mixed layer depth (solid line).

Our biological model describes dissolved inorganic nitrogen (*DIN*), phytoplankton biomass (*Phy*), phytoplankton chlorophyll (*Chl*), detritus (*Det*) and oxygen (*Oxy*) and is a simplified version of the model of Fennel et al. (2006). As illustrated in Fig. 2, the 3 nitrogen-based variables *DIN*, *Phy*, and *Det* describe a highly simplified nitrogen cycle while *Chl* and *Oxy* mainly serve diagnostic purposes.

The general equation for a biological variable C is

$$\frac{\partial C}{\partial t} - \frac{\partial}{\partial z}\left(K_t \frac{\partial C}{\partial z}\right) = SMS(C), \tag{1}$$

where K_t refers to the turbulent diffusivity and $SMS(C)$ denotes local sources minus sinks of C. The local sources and sinks of phytoplankton biomass are growth, mortality and sinking according to

$$SMS(Phy) = \mu(DIN, I, T)Phy - m_{Phy}Phy - w_{Phy}\frac{\partial Phy}{\partial z}. \tag{2}$$

The phytoplankton mortality rate m_{Phy} and the phytoplankton sinking rate w_{Phy} are constant, while the phytoplankton growth rate μ depends on the nutrient concentration *DIN*, the photosynthetically available light I and temperature T as follows

$$\mu(DIN, I, T) = \mu_{max}(T)\frac{\alpha I}{\sqrt{\mu_{max}^2 + \alpha^2 I^2}}\frac{DIN}{k_{DIN} + DIN}. \tag{3}$$

Here k_{DIN} is the half-saturation concentration for nutrient uptake, $\mu_{max}(T) = \mu_0 1.066^T$ is the temperature-dependent maximum growth rate, and α is the initial slope of the photosynthesis–irradiance curve. The photosynthetically available light at depth z is given by

$$I = I(z) = I_0\, par \exp(-z k_{water} - \int_0^z k_{Chl} Chl(\eta) d\eta), \tag{4}$$

where I_0 is the incoming light just below the ocean surface and $par = 0.43$ represents the fraction of light used in photosynthesis. The coefficients $k_{water} = 0.05\ m^{-1}$ and $k_{Chl} = 0.03$ (mg chlorophyll)$^{-1}$ m^{-1} account for light attenuation due to water and chlorophyll, respectively.

The source and sink terms of detritus are phytoplankton mortality, remineralization and vertical sinking:

$$SMS(Det) = m_{Phy}Phy - r_{Det}Det - w_{Det}\frac{\partial Det}{\partial z}, \tag{5}$$

where r_{Det} and w_{Det} are the remineralization and sinking rates of detritus, respectively.

The source and sink terms of *DIN* are detritus remineralization and nutrient uptake by phytoplankton:

$$SMS(DIN) = -\mu Phy + r_{Det}Det. \tag{6}$$

We included *Chl* as a separate state variable because the ratio of phytoplankton biomass to chlorophyll is known to vary dramatically with depth in oligotrophic waters such as the Sargasso Sea (Fennel and Boss, 2003). These variations are due to photoacclimation, the process by which phytoplankton cells regulate their internal chlorophyll levels depending on ambient light and nutrient conditions, and has been described mechanistically by Geider et al. (1996, 1997). The *Chl* equation:

$$SMS(Chl) = \rho_{Chl}\mu Phy - m_{Phy}Chl - w_{Phy}\frac{\partial Chl}{\partial z}, \tag{7}$$

follows directly from Eq. (2), but includes the factor ρ_{Chl} to account for photoacclimation. ρ_{Chl} is defined as

$$\rho_{Chl} = \frac{\theta_{max}\mu Phy}{\alpha I Chl}, \tag{8}$$

where θ_{max} is the maximum ratio of the chlorophyll to phytoplankton concentration and $\frac{\mu Phy}{\alpha I Chl}$ represents the ratio of achieved-to-maximum potential photosynthesis (Geider et al., 1997).

Oxygen is produced during photosynthesis, consumed during the remineralization of detritus and exchanged with the atmosphere at the sea surface. The oxygen sources and sinks are as follows:

$$SMS(Oxy) = r_{O_2:N}\mu Phy - r_{O_2:N} r_{Det} Det + \frac{vk_{O_2}}{h}(Oxy_{sat} - Oxy), \tag{9}$$

where $r_{O_2:N} = 8.625$ mol O_2/mol N is the oxygen to nitrogen stoichiometry, vk_{Oxy} is the gas exchange coefficient for oxygen, $h = 1\,m$ is the thickness of the topmost model layer, and Oxy_{sat} is the oxygen saturation concentration. The last term in Eq. (9) parameterizes the air–sea gas exchange and is only present in the model's top layer. The oxygen saturation concentration Oxy_{sat} is dependent on temperature and salinity and calculated following Garcia and Gordon (1992). We parameterized the gas exchange coefficient vk_{Oxy} after Wanninkhof (1992) as

$$vk_{Oxy} = 0.31\, u_{10}^2 \sqrt{\frac{660}{Sc_{Oxy}}}. \tag{10}$$

Here u_{10} is the wind speed 10 m above the ocean surface, and Sc_{Oxy} is the Schmidt number, calculated based on Wanninkhof (1992).

We initialized the model with BATS data of nitrate + nitrite, chlorophyll *a*, oxygen, temperature and salinity for October 1, 1989, and assumed an initially homogeneous concentration of 0.01 mmol N m^{-3} for phytoplankton biomass and detritus. We allowed the model to spin up for 3 months and then ran the simulations for 2 years from January 1, 1990 to December 31, 1991. During this period, additional data were available from the BATS bloom cruises which took place from January to April, coinciding with the annual phytoplankton bloom. The bloom cruises are in addition to the monthly core cruises and improve the temporal resolution of the bloom from monthly to bi-monthly or higher.

Initially we chose a set of biological parameters based on typical literature values, but then determined an optimal set of biological parameters by minimizing the misfit between model-predicted and observed values of PON (*Phy* + *Det*) and *Chl* using a genetic algorithm (Mattern, 2008). The biological parameters before and after the optimization are listed in Table 2.

The simulated biological variables are shown in comparison with the observations in Fig. 3. The model displays the typical seasonal cycle, with deep mixing events during late winter and early spring that provides the surface region with a supply of nutrients and fuels a surface phytoplankton bloom. During the rest of the year phytoplankton in the top 80 m, where light is abundant, is mainly nutrient-limited and a deep chlorophyll maximum establishes itself at the base of the euphotic zone. Oxygen is generally higher in the top 100 m, where net oxygen production occurs due to photosynthesis, and decreases at depth due to remineralization of sinking organic matter. During summer, when water temperatures in the shallow mixed layer reach values of 26 °C and higher, oxygen outgasses from the ocean due to reduced solubility.

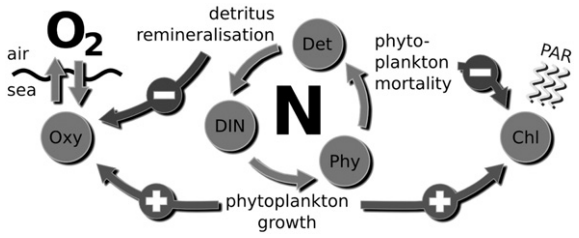

Fig. 2. Schematic of the biological model component.

Table 2
Biological model parameter set before and after parameter optimization.

Name	Value		Unit	Description
	Before	After		
m_{Phy}	0.05	0.05	d^{-1}	Phytoplankton mortality rate
μ_0	1.0	0.5	d^{-1}	Maximum phytoplankton growth rate for $T=0$ °C
r_{Det}	0.02	0.0414	d^{-1}	Detritus remineralization rate
k_{DIN}	0.5	0.7	mmol N m^{-3}	Half-saturation concentration of DIN uptake
α	0.075	0.25	$\frac{\text{mmol N}}{\text{mg chlorophyll d W m}^{-2}}$	Initial slope of the photosynthesis–irradiance curve
θ_{max}	3.84	6.0	$\frac{\text{mg chlorophyll}}{\text{mmol N}}$	Maximum ratio of chlorophyll to phytoplankton concentration
w_{Phy}	−0.08	−0.1	m d^{-1}	Sinking rate of phytoplankton
w_{Det}	−0.8	−0.2029	m d^{-1}	Sinking rate of detritus

For the purpose of sequential assimilation we performed ensemble runs of the model. The ensemble members use identical initial and forcing data, but differ in their biological parameters, a subset of which we perturbed randomly and independently around the optimal parameter set assuming a log-normal distribution. We used the log-normal distribution because it is non-negative, thus preventing negative parameter values, and because it is skewed, thus allowing large parameter values well above the mean to be drawn occasionally. We chose the particular subset of stochastic parameters (Table 3) based on a sensitivity analysis (Mattern, 2008). The distributional parameters for the log-normal distributions were based on the optimal values to specify the mean and plausible range of their variation to set the variance.

The mean of our stochastic ensemble simulations is similar to the deterministic run. As one would expect, the variance of the ensemble is small below 150 m, where phytoplankton growth is not possible due to insufficient light. The ensemble variance is maximum at the nutricline (see Fig. 1 of Supplementary Online Material).

3. Sequential data assimilation using ensemble methods

The state of our biological system at any time is defined by the vector X containing all the biological variables, at all the model grid points, i.e.

$$X = (Phy_1,\ldots,Phy_{350},Det_1,\ldots,Det_{350},\\ DIN_1,\ldots,DIN_{350},Chl_1,\ldots,Chl_{350},Oxy_1,\ldots,Oxy_{350})', \quad (11)$$

where the subscripting on each variable represents the vertical grid cell index. (Any explicit dependence on time is suppressed at this stage.) Therefore, X is a 5 (variables) × 350 (layers) = 1750 × 1 dimensional vector (the superscript $'$ represents the matrix transpose). There is no feedback from biology to the physical model, so physical variables are not part of the state vector. The forecast ensemble generation outlined above produces a set of n_{ens} state vectors at any time of interest, which is denoted as $\{X^{(i)}\}_{i=1}^{n_{ens}}$, where i is the numerical identifier for a particular ensemble member. (Note that the curly braces denote the full ensemble, and when they are omitted we are referring to an individual ensemble member.)

Ensemble-based sequential data assimilation estimates the system state as it evolves through time, approximating the probability density function of the system state by an ensemble that represents a sample whose properties reflect the distributions of interest (Ristic et al., 2004). More precisely, sequential ensemble methods approximate the probability distribution (or its moments) of the nowcast state using all available measurements up to and including the analysis time. We designate these as $y_{1:\tau}=(y'_1,y'_2,\ldots,y'_\tau)'$, where the individual y_t are column vectors of the available observations at time t. Following convention, the time index has integer values $t=1,2,\ldots,\tau$ that correspond to the times at which observations are available; this time indexing will also be incorporated as a subscript on X.

Consider the single stage transition of the system from one observation time to the next, i.e. time $t-1$ to t. This is a 2-step process involving prediction and update (or assimilation). Starting with the nowcast at time $t-1$, the state of the system can be described by the probability distribution of X_{t-1} given all observations, $y_{1:t-1}$, up to time $t-1$; this is designated $p(x_{t-1}|y_{1:t-1})$. The prediction step then performs a forecast using this initial condition, i.e. it transforms the nowcast $p(x_{t-1}|y_{1:t-1})$ into the forecast distribution $p(x_t|y_{1:t-1})$, which is the probability distribution of X_t given observations up to $t-1$. When the new observations y_t become available at time t, the assimilation step updates the forecast using the additional information in y_t, which yields $p(x_t|y_{1:t})$, the nowcast distribution at time t. This new nowcast is then used as the starting point for the next prediction step and so on, sweeping forward through time (for more details, see Dowd, 2007).

For the assimilation step, the probability distribution required is the forecast distribution $p(x_t|y_{1:t-1})$, which is approximated by the forecast ensemble $\{X^{(i)}_{t|t-1}\}_{i=1}^{n_{ens}}$. This forecast ensemble is produced by the stochastic simulation that started with an ensemble characterizing the nowcast at time $t-1$ ($\{X^{(i)}_{t-1|t-1}\}_{i=1}^{n_{ens}}$), as described in Section 2. With the extra information available at time t, via the new observation y_t, the nowcast probability distribution $p(x_t|y_{1:t})$ becomes the desired target quantity, approximated by an associated nowcast ensemble $\{X^{(i)}_{t|t}\}_{i=1}^{n_{ens}}$. SIR and the EnKF are Monte Carlo algorithms that transform the forecast ensemble $\{X^{(i)}_{t|t-1}\}_{i=1}^{n_{ens}}$ into the desired nowcast ensemble $\{X^{(i)}_{t|t}\}_{i=1}^{n_{ens}}$. Both procedures are outlined below.

In our case, the observations y_t can be related to the system state through a linear equation of the form

$$y_t = H_t X_t + v_t, \quad (12)$$

where H_t is a matrix that maps between the observations and the model state vector. The additive noise v_t is assumed to follow a normal distribution with zero-mean and covariance matrix R, or $v_t \sim N(0,R)$. The construction of H_t is straightforward. Most observations are direct measurements of the biological variables; hence, H_t maps those variables onto the corresponding spatial grid of the observations, except for the model variables phytoplankton and detritus, the sum of which corresponds to the observed quantity PON. Thus, H_t maps the vector entries of both phytoplankton and detritus onto the corresponding PON index in the observation vector.

3.1. The ensemble Kalman filter

The EnKF is based on the Kalman filter update equations. The update step of the EnKF that generates the nowcast ensemble is

$$\tilde{X}^{(i)}_{t|t} = \tilde{X}^{(i)}_{t|t-1} + K_t\left(Y^{(i)}_t - H_t\tilde{X}^{(i)}_{t|t-1}\right) \quad \text{for } i = 1,2,\ldots,n_{ens} \quad (13)$$

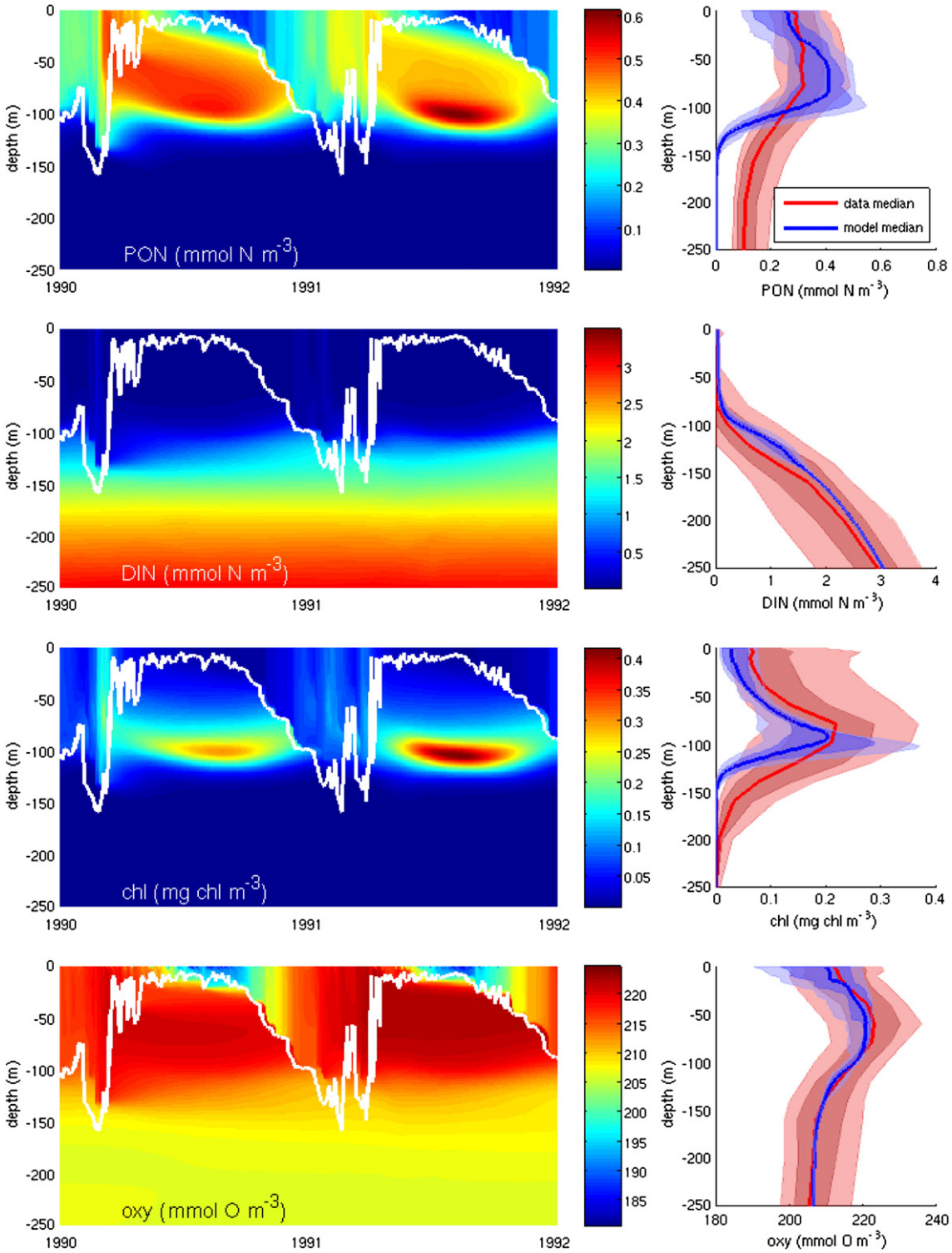

Fig. 3. Model-simulated development of PON, DIN, chlorophyll and oxygen (left panels) and a comparison between their time-integrated depth distributions with observations (right panels) from January 1, 1990, to January 1, 1992. Median (solid lines), area between 0.1 and 0.9 quantile (light shaded area) and between 0.25 and 0.75 quantile (dark shaded area) are shown for model (blue) and observations (red).

and is applied to each ensemble member separately. Essentially, the so-called gain matrix K_t incorporates an increment based on a data-model discrepancy to update the forecast state. The resultant set $\{\tilde{X}_{t|t}^{(i)}\}_{i=1}^{n_{ens}}$ forms the new nowcast ensemble. The tilde notation is used here to emphasize that in general these are samples from an approximation of the target distribution, not the exact target distribution $p(x_t|y_{1:t})$. The EnKF requires an ensemble of observations generated as $Y_t^{(i)} = Y_t + v_t^{(i)}$, $i = 1,\ldots,n_{ens}$, with $v_t^{(i)}$ being an independent draw from $N(0,R)$. The Kalman gain matrix is computed as

$$K_t = PH'_t(H_tPH'_t + R)^{-1}, \tag{14}$$

Table 3
Log-normal distributions of biological parameters that vary during stochastic simulations.

Name	Distribution	Expected value	Name	Distribution	Expected value
m_{Phy}	Log-N(−3.4957, 1.0)	0.05	α	Log-N(−1.8863, 1.0)	0.25
μ_0	Log-N(−1.1931, 1.0)	0.5	θ_{max}	Log-N(1.2918, 1.0)	6.0
r_{Det}	Log-N(−3.6845, 1.0)	0.0414	$-w_{Phy}$	Log-N(−2.8026, 1.0)	0.1
k_{DIN}	Log-N(−0.8567, 1.0)	0.7	$-w_{Det}$	Log-N(−2.0995, 1.0)	0.2029

To ensure that the sinking rates w_{Phy} and w_{Det} are negative, $-w_{Phy}$ and $-w_{Det}$ follow a log-normal distribution.

where P is the sample covariance matrix generated from the forecast ensemble $\{\tilde{X}_{t|t-1}^{(i)}\}_{i=1}^{n_{ens}}$. For more details on the EnKF, see Evensen (2003, 2006).

3.2. Sequential importance resampling

During the SIR update step at time t a weight (or probability), designated $\hat{w}_t^{(i)}$, is assigned to each forecast ensemble member, $X_{t|t-1}^{(i)}$, according to its likelihood, thereby reflecting the fidelity of $X_{t|t-1}^{(i)}$ to the observations y_t. The forecast ensemble, $\{X_{t|t-1}^{(i)}\}$, is then resampled, with replacement, where members are drawn with a probability proportional to their weight (in other words, a weighted bootstrap). This produces the new nowcast ensemble $\{X_{t|t}^{(i)}\}$. Thus, the SIR algorithm works by preferentially selecting the forecast ensemble members with high weights, which are, in practice, those profiles closest to the available observations. In contrast, ensemble members far from observed values (and hence with low weights) are more likely to drop out of the ensemble during resampling. An overview of SIR (also referred to as particle filtering) is given by Ristic et al. (2004).

The weight $\hat{w}_t^{(i)}$ for the forecast ensemble member $X_{t|t-1}^{(i)}$ is determined according to the likelihood

$$\hat{w}_t^{(i)} = p(y_t|X_{t|t-1}^{(i)}) \text{ for } i = 1,2,\ldots,n_{ens} \tag{15}$$

which is the probability that the observation derives from forecast ensemble member i. The weights are then normalized such that their sum is 1 and they reflect the resampling probability. Finally, the nowcast ensemble is generated by sampling from the forecast ensemble according to the calculated probabilities. Resampling proceeds by creating an empirical cumulative distribution function from the normalized weights which provides a basis for weighted bootstrapping with replacement (see Arulampalam et al., 2002).

A likelihood function must also be specified. Both the parametric form of this distribution, as well as the numerical values for its parameters are important. Here, we use a likelihood based on a multivariate normal distribution

$$p(y_t|X_{t|t-1}^{(i)}) \propto exp\left(-\frac{1}{2}(y_t - H_t X_{t|t-1}^{(i)})' \Sigma^{-1} (y_t - H_t X_{t|t-1}^{(i)})\right), \tag{16}$$

where Σ is the covariance matrix of the errors between observations and forecast values. For simplicity, Σ was considered here a diagonal matrix with elements corresponding to the sample variances obtained for each of the measured variables. In practice, we found that the results were sensitive to the specification of these observation error variances since they controlled the spread (or range of the values) of the weights that govern the resampling step. With too much spread, sample degeneracy and ensemble collapse can occur (i.e. only a small number of the resampled ensemble members are distinct from one another, many are repeated); with too little spread the forecast ensemble is not altered by the assimilation or update step. In lower dimensional problems, parameters of the likelihood function (such as the observation error variance) can be estimated using modified SIR procedures (Kitagawa, 1998).

Here we generate ensembles mainly by perturbing the biological parameters. The resultant set of vertical profiles on all variables is resampled, so that each ensemble member satisfies the dynamical equations (conditional on the parameter set). We refer to this as our All Variables SIR method. A potential drawback to the enforcement of dynamical balance is that resampling selects the profiles of all variables based on a global likelihood Eq. (16). This means that a bad fit in 1 variable (e.g. *Chl*) can be compensated for by a good fit in another variable (e.g. PON). In order to assess the effect of this constraint, we also use a modified implementation of SIR that considers each variable separately. This means that profiles of each variable are selected independently based only on its observations. The resulting resampled profiles are then rejoined to form the nowcast ensemble. (In terms of Eq. (16), this means that the likelihood would be evaluated at time t for a subset of measurements on one variable type and H_t altered accordingly; the profiles associated with that variable would then be sampled according to this simplified likelihood.) We refer to this as Separate Variables SIR. The motivation for this was to bridge the All Variables SIR, which is dynamically consistent, with the EnKF, which does not satisfy dynamical balance, but allows for improved fitting to observations through an incremental update to the model state.

4. Results

4.1. Nowcast results

Simulation results after application of sequential assimilation are shown for the EnKF (Fig. 4) and the SIR (Fig. 5). In both cases, the evolution of the prognostic variables over time is consistent with the corresponding results for the deterministic model (Fig. 3). However, the perturbations resulting from the assimilative updating of the ensemble are clearly evident in the mean and standard deviation for both data assimilation procedures. The perturbations result from the discrepancy between forecast ensemble and observations at each assimilation step, during which the mean and the variance are shifted. This is a characteristic feature of all sequential online estimation procedures. For the SIR, the ensemble members in the nowcast ensemble are a subset chosen from the forecast ensemble; hence, the ensemble does not move out of the boundaries set by the ensemble forecast. The EnKF update, on the other hand, allows for larger shifts in the ensemble distribution. For these reasons, the SIR update in Fig. 5 appears less severe, in particular for PON and *Chl*, and produces a smoother predicted state than the EnKF (Fig. 4). The standard deviation is more strongly reduced during each update of our EnKF implementation than during the SIR update. For the SIR, increases in standard deviation at update are possible, as is the case for PON in the later half of 1991 (Fig. 5). This result occurs in combination with a decrease in standard deviation for other variables or other regions in the model.

The time-series plots of the variables at the surface (depth-averaged upper 80 m) in Figs. 6 and 7 illustrate the temporal changes in the ensemble distributions. The mean and variance shifts are evident at the assimilation times. Also, the stronger effect of the EnKF update in comparison to the SIR update is readily observable. The difference is especially obvious for PON in the assimilation step in April 1991; the mean observation for PON is much higher than the ensemble mean, causing a strong shift during the assimilation step.

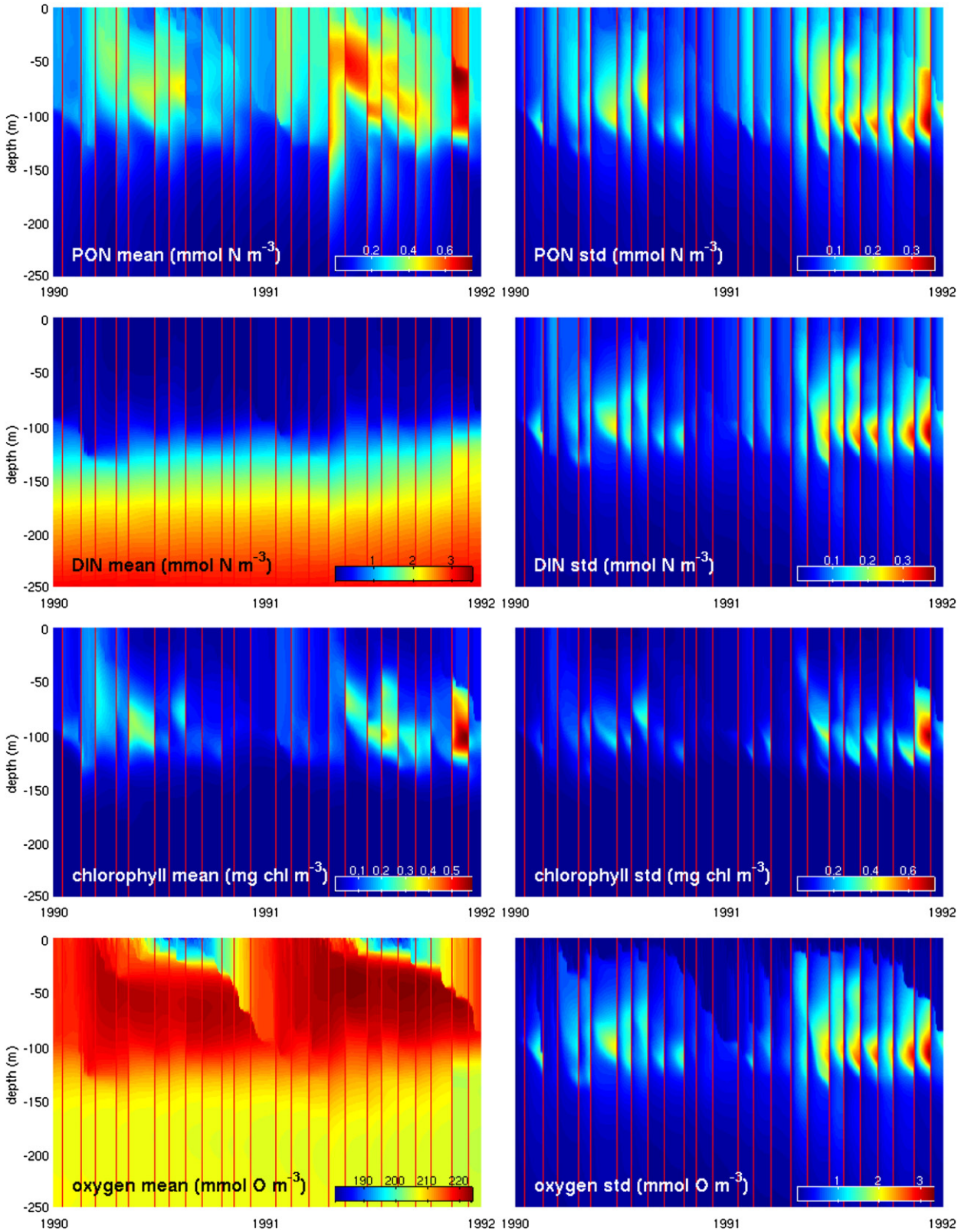

Fig. 4. Time-depth plots of the ensemble mean (left panels) and its standard deviation (right panels) for a 40 member ensemble run and EnKF data assimilation. Red vertical lines mark the assimilation steps.

While the EnKF update elevates the ensemble mean to a level beyond the previous ensemble maximum and very close to the observations, this is not possible in our SIR procedure, which leaves the ensemble closer to the model state prior to the update. The strength of this effect during the EnKF update depends primarily on the uncertainty in observations relative to that of the model state. Consequently, our specification of the observation errors is important. If a low uncertainty (a noise distribution with a low variance) is assigned to the observations, the EnKF update will have a relatively strong effect and move the model state closer to the data. For a high uncertainty,

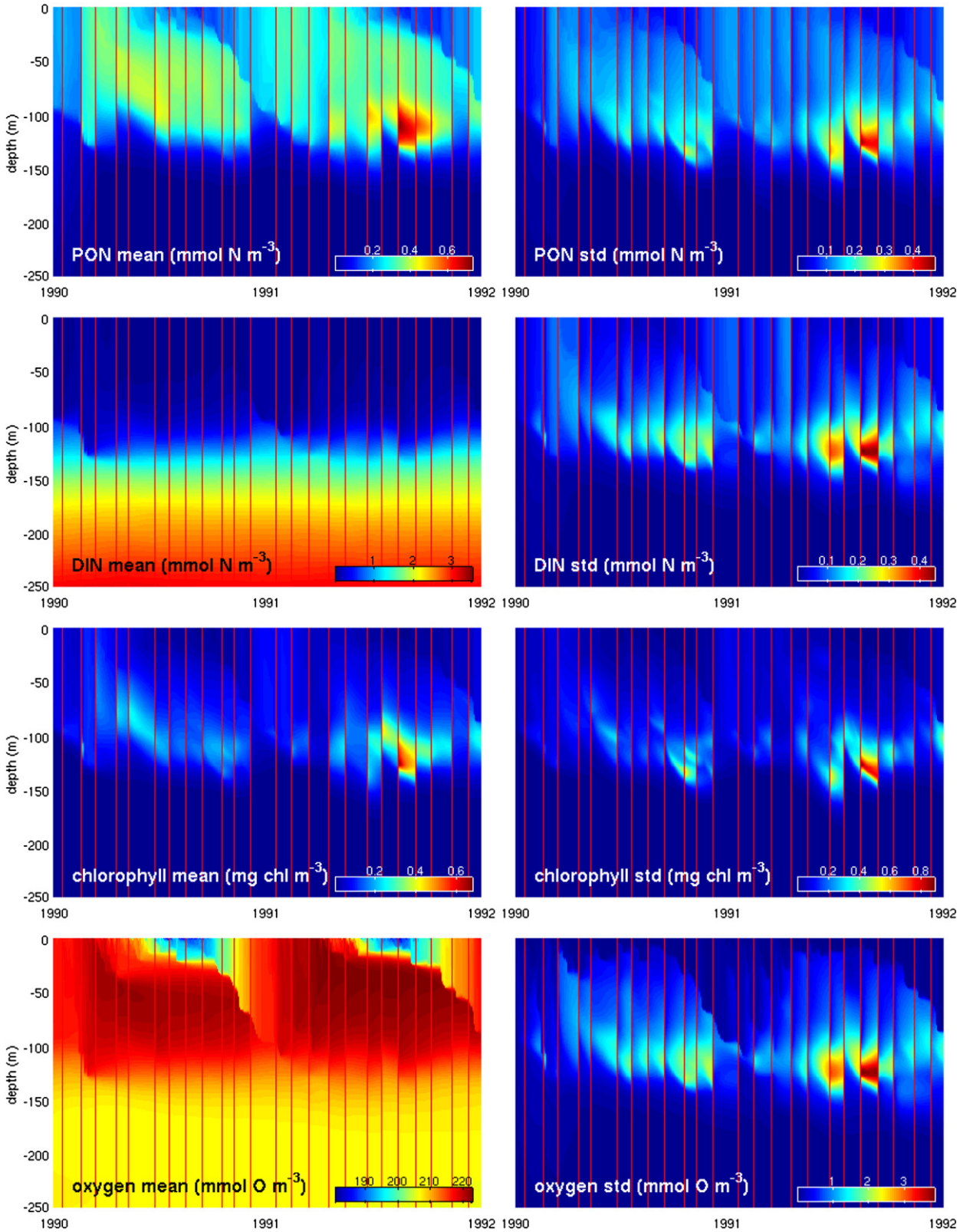

Fig. 5. As in Fig. 4 but for SIR.

the updated ensemble will stay closer to its initial state prior to assimilation. It is therefore meaningless to compare model and observations directly after the assimilation is performed, as the EnKF can be adapted to fit the data almost perfectly. A more instructive approach is to compare the results of EnKF and SIR by assessing their predictive skill. This is done below.

4.2. Forecast skill

Our data assimilation results in Figs. 6 and 7 suggest that alterations of the model state (or its ensemble representation) due to assimilating observations at a monthly time step may not improve the forecast one month into the future. Comparing the deterministic

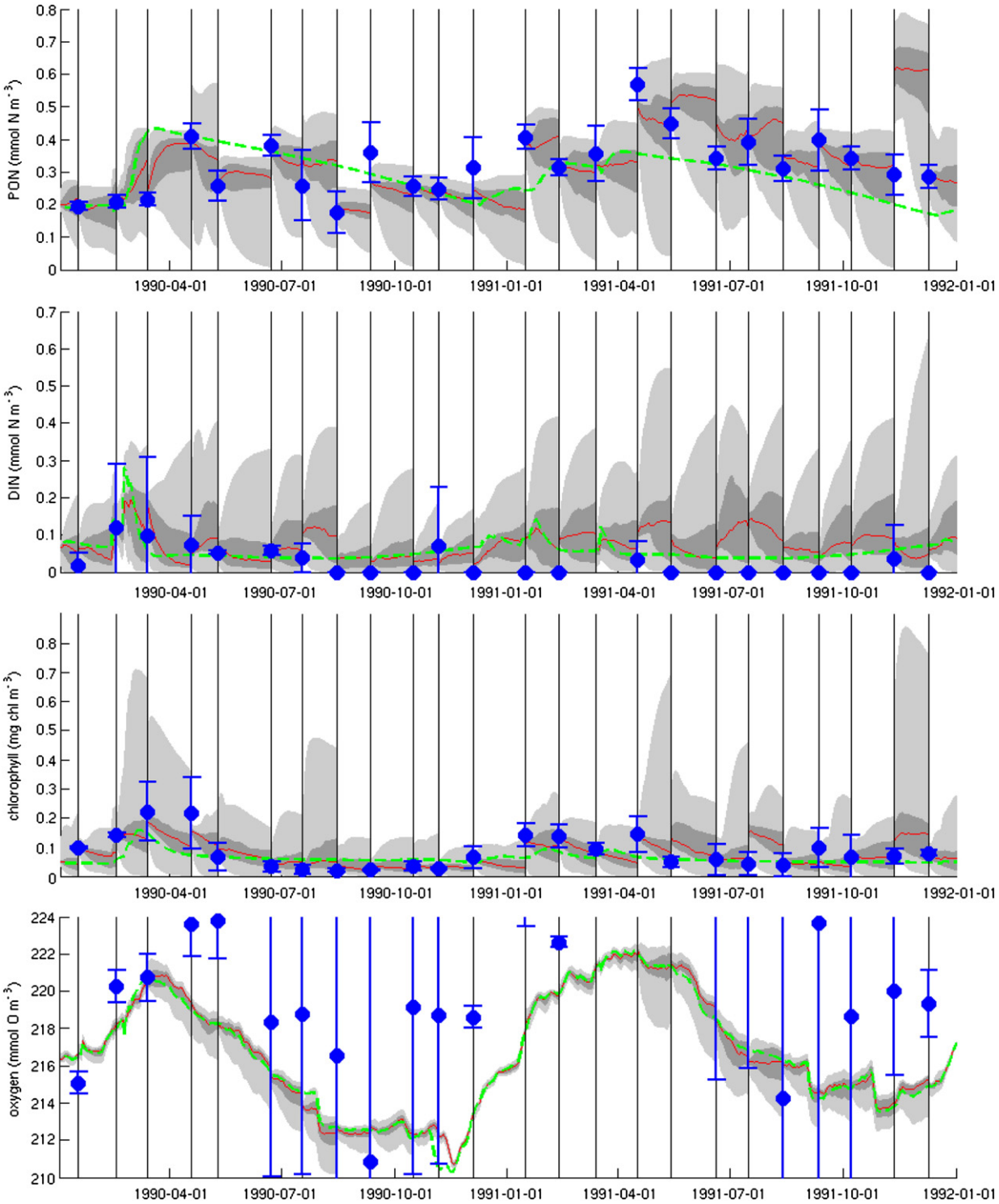

Fig. 6. Ensemble distribution of the mean concentration of PON, DIN, chlorophyll and oxygen in the top 80 m with EnKF data assimilation. The solid red line is the ensemble median, the dark gray area shows the regions between 0.25 and 0.75 quantile, and the light gray area marks the region between the ensemble minimum and maximum. EnKF assimilation steps are marked by black vertical lines. Blue dots and error bars show the mean observations and their standard deviation in the top 80 m. Deterministic model run is shown as a green dotted line.

simulation (green dashed line) and the ensemble median (red solid line), it appears that between the monthly BATS sampling dates the model reverts back to a state close to that achieved without data assimilation. This was also demonstrated with cross-validation experiments (Mattern, 2008, results not shown). In order to assess the predictive skill of our assimilation schemes at a shorter time scale, we make use of the BATS bloom cruise data. The bloom cruises were intensive sampling periods in which observations were collected between the dates of the monthly regular core cruises. For the purposes of assessing forecast skill, we use the bloom cruise data purely as validation data and not as part of the data assimilation procedure. Specifically, we compute the root mean square error (RMSE) between the validation data and the predicted model output for those times (corresponding to a roughly 2 week forecast). These

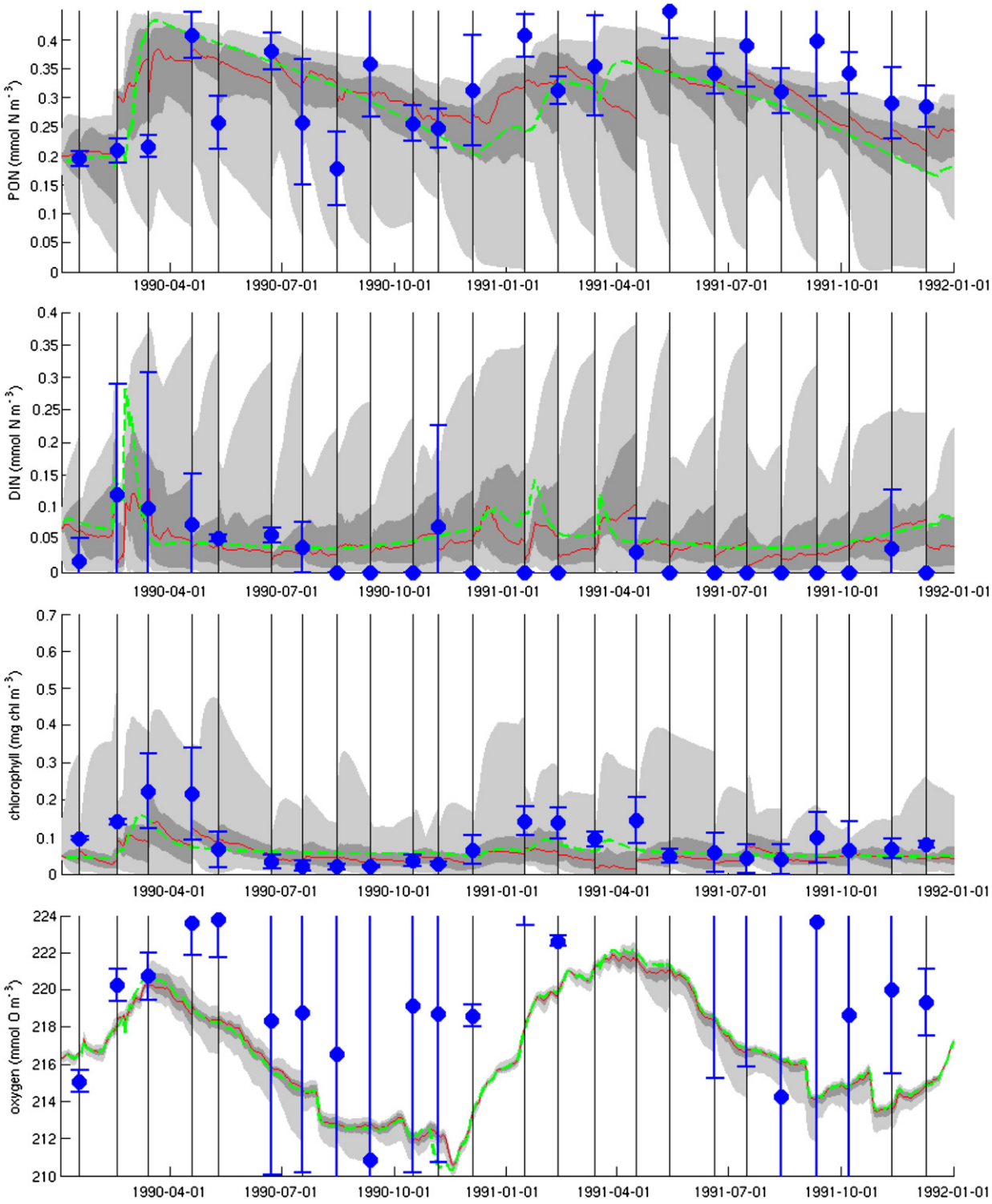

Fig. 7. As in Fig. 6 but for SIR.

RMSEs are computed for the deterministic model run, as well as for our EnKF implementation and the 2 SIR implementations introduced in Section 3.2. This is done for each data assimilation technique and for different ensemble sizes, namely $n_{ens} = 5$, 10, 20, 40, 80, and for each of the prognostic variables. The results are shown in Table 4. In each case, 20 replicate runs were carried out so that the standard deviation of the RMSE results could be computed and the Monte Carlo variation assessed.

The results in Table 4 demonstrate that a significant improvement in the predictive ability of the biological model can be achieved with both the EnKF and SIR procedures. The improvement is most evident for *Chl* (using the EnKF and the Separate Variables SIR implementation), as well as for PON (using the EnKF). The stronger updating of the ensemble mean towards the observations by the EnKF data assimilation appears to lead to a more positive impact on the predictive skill; the EnKF results for ensemble sizes greater than 10 are better than the equivalent SIR results, especially for PON. It is notable that the model results for oxygen cannot be significantly improved by any of the data assimilation techniques. This is consistent with the result of our stochastic simulations, where the variation of

Table 4
Root mean square error (RMSE) between BATS bloom observations and corresponding model output for the deterministic model with the optimized parameter set and for 3 assimilation implementations and different ensemble sizes.

n_{ens}	EnKF	SIR	SIR (separate)	Deterministic
PON (mmol N m^{-3})				
5	0.187 ± 0.019	0.200 ± 0.012	0.210 ± 0.017	0.198
10	0.176 ± 0.008	0.197 ± 0.012	0.200 ± 0.011	
20	0.173 ± 0.006	0.191 ± 0.006	0.190 ± 0.010	
40	0.172 ± 0.005	0.190 ± 0.007	0.190 ± 0.008	
80	0.172 ± 0.003	0.192 ± 0.008	0.184 ± 0.008	
DIN (mmol N m^{-3})				
5	0.735 ± 0.024	0.761 ± 0.014	0.752 ± 0.021	0.757
10	0.732 ± 0.023	0.754 ± 0.011	0.748 ± 0.016	
20	0.730 ± 0.019	0.756 ± 0.006	0.752 ± 0.015	
40	0.740 ± 0.018	0.752 ± 0.006	0.754 ± 0.015	
80	0.742 ± 0.012	0.753 ± 0.005	0.751 ± 0.012	
Chlorophyll (mg chlorophyll a m^{-3})				
5	0.092 ± 0.007	0.113 ± 0.011	0.110 ± 0.011	0.104
10	0.096 ± 0.007	0.112 ± 0.009	0.103 ± 0.010	
20	0.094 ± 0.005	0.110 ± 0.007	0.096 ± 0.006	
40	0.093 ± 0.003	0.110 ± 0.006	0.096 ± 0.004	
80	0.093 ± 0.002	0.111 ± 0.004	0.094 ± 0.004	
Oxygen (mmol O m^{-3})				
5	9.343 ± 0.261	9.359 ± 0.098	9.493 ± 0.244	9.350
10	9.294 ± 0.229	9.328 ± 0.103	9.451 ± 0.129	
20	9.277 ± 0.165	9.296 ± 0.078	9.516 ± 0.150	
40	9.342 ± 0.135	9.255 ± 0.075	9.561 ± 0.157	
80	9.339 ± 0.105	9.254 ± 0.081	9.549 ± 0.168	

Each cell contains the mean and standard deviation of 20 ensemble runs. n_{ens} is the ensemble size.

the chosen biological parameters did not create a large ensemble spread for oxygen (see Supplementary Online Material). The comparison between the 2 different SIR implementations reveals that the standard All Variables SIR implementation produces results as good as those produced by the Separate Variables SIR, except for *Chl* where the latter technique performs better.

Ensemble size is a key practical consideration in sequential data assimilation, trading off accuracy against computational cost. Table 4 also considers the predictive skill using various ensemble sizes, including an assessment of the Monte Carlo variability of the results through replicate runs. For very small ensembles, with 5 or 10 ensemble members, the predictive skill is poorer and the replication error (standard deviation) larger, especially for the EnKF. Increasing the ensemble size decreases the prediction error and its standard deviation. However, it is seen that for ensemble sizes of 20 and greater, a doubling of the ensemble size does not change the predictive skill significantly but doubles the computational cost (which scales linearly with ensemble size). However, the increase in ensemble size shows a positive effect on the standard deviation; for most variables it decreases at a rate roughly equal to the inverse square root of the ensemble size.

Another important feature in the assimilation of multivariate time-series data is illustrated in our application. Consider that the performance of our standard (All Variables) SIR implementation for *Chl* in Table 4 is poor compared to the other 2 implementations. This indicates that the chlorophyll profiles are resampled disadvantageously during the SIR's update step. In the SIR update procedure, ensemble members can have a high probability of being resampled if a poor fit for certain variables is compensated by a good fit for other variables. In our case, poor chlorophyll profiles are resampled in combination with good PON profiles. This is likely indicative of dynamical inconsistencies in the biological model formulation. In the application of the EnKF for multivariate data assimilation the generation of new ensembles allows the fit to improve for all variables.

Finally, note that the results presented here are based on parameter variation following a specific log-normal distribution (Table 2). Experiments with other probability distributions, e.g. a truncated Gaussian, showed that the results are quite sensitive to the distribution chosen (Mattern, 2008). Since it is often difficult to assign these distributions accurately, we remark briefly on the consequences of their mis-specification. At a basic level, the SIR procedure needs a sufficient forecast ensemble spread, and thus requires an appropriate parameter distribution, to support this feature. This idea is illustrated in Figs. 6 and 7, where at the observation (or assimilation) times the forecast spread generally brackets the observation (or, in the case of oxygen, the forecast ensemble spread and the observation error bars overlap). If the ensemble spread is too small, the resampling step in the SIR leads only to limited improvement and the result suffers. This implies, however, that the model errors have been underestimated. The EnKF, on the other hand, can transform the ensemble out of its previous range upon update, even if model errors have been underestimated. The EnKF, however, is more sensitive to both observational data outliers and ensemble outliers. For the former, the EnKF will force the ensemble to trend towards extreme observations. In the latter case, where an improbable combination of extreme parameters produces an ensemble outlier, e.g. unrealistic profiles, the outcome of the EnKF update can be affected detrimentally, especially for small ensemble sizes. (We encountered this during one EnKF ensemble run where we had to remove an extremely high chlorophyll profile from the analysis.) The SIR is a more robust procedure in this respect, as ensemble outliers that are far from the data are assigned a low weight during the resampling step, and hence are unlikely to be propagated forward.

5. Discussion and conclusions

In this study we examined the application of 2 major sequential data assimilation techniques, the EnKF and SIR to a 1D coupled physical–biological ocean model for the long-term ocean monitoring site off Bermuda (BATS, Steinberg et al., 2001). We choose the 1D model as a compromise between realism in describing the biology and physics of our test site versus the computational considerations inherent in these ensemble-based Monte Carlo methods. To date, the EnKF has found a wider range of applications in the context of biological models (e.g. Allen et al., 2003; Natvik and Evensen, 2003; Lenartz et al., 2007), whereas the SIR has been used less frequently and in the context of simpler 0D models (Losa et al., 2003; Dowd, 2007). The novelty of this study hence lies in its use of SIR for data assimilation in a partial differential equation based physical–biological model, and its comparison and contrast with the EnKF, in the context of estimation and prediction. However, the approaches considered here should be scaleable to higher dimensional problems, e.g. the ocean general circulation model used for ensemble-based data assimilation by Brusdal et al. (2003).

In our implementation of sequential data assimilation, we have focused on the biological components only. The physical–biological coupling in our model is one-way: the physical model affects biological distributions through turbulent mixing, but the biological variables do not feed back to the model physics. With nudging of model temperature and salinity to the time-series observations from the BATS site, the physical model is able to adequately recreate key physical features such as the mixed layer depth; this suggests that the model can be useful for short-term predictions of biological properties at the BATS site. As an extension, the distribution and time evolution of the biological variables also contain information that could refine the physical state, say by appending the state to include physical variables as well as biological ones.

We proceeded with ensemble generation by considering variations in a subset of the biological parameters (chosen based on a sensitivity analysis) as a dominant source of uncertainty or error (Lek,

2007). After assigning probability distributions (log-normals) to these parameters, we sampled randomly from these in order to generate ensemble members. See Turner et al. (2008) for a general discussion on ensemble generation and error incorporation. Joint state and parameter estimation is also possible for stochastic dynamics. For SIR, state augmentation approaches for this have been developed (Kitagawa, 1998; Ionides et al., 2006); for the EnKF, similar methods are also possible (Annan et al., 2005; Moradkhani et al., 2005).

After ensemble generation, the EnKF and SIR provide an update step to assimilate available observations. While both procedures can be readily applied to a biological model, they operate quite differently. The EnKF incrementally updates the model state through the matrix-based Kalman filter updating equations (Evensen, 2006), while SIR is a weighted bootstrap procedure based on a likelihood function (Ristic et al., 2004). Note that these nonlinear filtering problems are distinct from fully Bayesian approaches which assign priors to parameters and rely on computationally intensive Markov Chain Monte Carlo (MCMC) algorithms (e.g. Dowd and Meyer, 2003).

In both techniques, one must carefully consider implementation details, such as the scaling (or sample variances) assigned to the observations and model outputs, otherwise a single variable type or observation can dominate the analysis. For the EnKF, the error covariance matrix of the forecast ensemble was formed and the matrix-based updating equation applied. For SIR, the likelihood function was defined on the basis of a multivariate normal distribution and resampling was done on the ensemble of profiles; it is possible that more suitable distributions could be identified that take better account of the discrepancy between observed and modelled profiles. In fact, a key feature of a successful SIR with small ensemble sizes is that the forecast distribution must overlap with the likelihood; this depends on both the parameter variation in the stochastic simulation, as well as the assigned observation error variance.

Our experiments used real time-series data from BATS. This is challenging since outliers are inevitably present, as are biases due to the model's inability to explain all features present in the observations. Both procedures appear robust. We also considered different implementations of SIR. In our All Variables SIR implementation, ensemble members are resampled to preserve the relations between the biological variables. In our Separate Variables SIR, we resampled each of the biological variables individually and independently at the cost of losing the dependencies between the variables during the update, in order to investigate a possible improvement in fit.

Our data assimilation experiments showed differences in performance between our implementations of the EnKF and the SIR. When compared to SIR, the EnKF update had a more pronounced effect in changing the ensemble from forecast to update; the mean was shifted more and the standard deviation was greatly reduced after the update. One reason for this is that the SIR update does not generate new ensembles (it simply resamples with replacement from the set of candidates provided by the forecast), whereas the EnKF generates a new set of ensemble members.

We investigated the effect of ensemble size, as it is a key determinant for performance. Generally we anticipate that larger ensembles give better answers (i.e. more samples better characterize the target distributions, or its moments), but they come at a higher computational cost. Our ensemble sizes ranged from 5 to 80. As a lower bound, we found that ensembles of 10 or fewer members are too small for reliable results. On the other hand, increasing the ensemble size above 20 resulted in only a slight decrease in error between the model output and the observations, suggesting that 20 is the optimal ensemble size for our application. We anticipate that the optimal ensemble size is specific to each application and may be higher for 3-dimensional models. Previously published studies that have applied the EnKF to coupled physical–biological models have used ensemble sizes of 100 to 200 (Allen et al., 2003; Evensen, 2003); ensemble forecasts in numerical weather prediction typically use fewer than 100 ensemble members (Gneiting and Raftery, 2005).

Our experiments indicate that the predictive skill improved for a 2-week forecast for both the EnKF and SIR in comparison to the deterministic model run. We assessed the forecast ability by comparing model output to observations obtained during intensive sampling periods when approximately bi-weekly data was available. The results suggest that the strong update of the model state closer towards observations in our EnKF implementation has a positive effect on the predictive skill. We also found that the forecast skill of our standard SIR procedure can be improved by resampling each variable separately. The improvement in forecast skill is variable-dependent. Forecasts of PON and chlorophyll profit most from the data assimilation, while no measurable improvement for oxygen was found.

The forecast skill of our application could likely be improved by reducing dynamical inconsistencies between our model and the BATS system. The 1D model is not able to capture some of the complex physical dynamics present at the BATS site, such as the influence of mesoscale eddies (McGillicuddy et al., 1998), and the biological dynamics have been highly simplified. Another important factor is the uncertainty assigned to the BATS observations, which is not accurately known. We approximated this uncertainty based on the variability in the observations. Both procedures are affected by this observation uncertainty — the EnKF through the observation error covariance matrix and the SIR through the likelihood specification. These control how closely the ensemble can move toward the observations at the update step.

In summary, the SIR and the EnKF improved model results and forecast abilities for the coupled physical–biological system we examined. Several choices had to be made during the application of both assimilation techniques to a specific system, e.g. the observation error covariance matrix and the likelihood function, which affect assimilation performance. In order to utilize the full improvement in the predictive skill that sequential data assimilation can offer, the model under consideration should be both well-calibrated (e.g. through parameter optimization) and also consistent with the system of interest. For the BATS site, future work would therefore begin by refining the physical and biological structure of the model. Our results however demonstrate that ensemble-based data assimilation is a promising direction for improving prediction in coupled physical–biological systems.

Acknowledgments

Katja Fennel and Paul Mattern were supported by ONR MURI grant N00014-06-1-0739. Paul Mattern was also supported by National Program for Complex Data Structures (NPCDS). Mike Dowd was supported by both NSERC and NPCDS. We thank Jill Falkenberg for her assistance in preparing BATS data for assimilation. We also thank two anonymous reviewers for constructive comments.

Appendix A. Supplementary data

Supplementary data associated with this article can be found, in the online version, at doi:10.1016/j.jmarsys.2009.08.004.

References

Allen, J., Eknes, M., Evensen, G., 2003. An Ensemble Kalman Filter with a complex marine ecosystem model: hindcasting phytoplankton in the Cretan Sea. Annales Geophysicae 21 (1), 399–411.

Annan, J., Hargreaves, J., Edwards, N., Marsh, R., 2005. Parameter estimation in an intermediate complexity earth system model using an ensemble Kalman filter. Ocean Modelling 8 (1–2), 135–154.

Arhonditsis, G., Brett, M., 2004. Evaluation of the current state of mechanistic aquatic biogeochemical modeling. Marine Ecology Progress Series 271, 13–26.

Arulampalam, M., Maskell, S., Gordon, N., Clapp, T., Sci, D., Organ, T., Adelaide, S., 2002. A tutorial on particle filters for online nonlinear/non-GaussianBayesian tracking. IEEE Transactions on Signal Processing 50 (2), 174–188.
Bertino, L., Evensen, G., Wackernagel, H., 2003. Sequential data assimilation techniques in oceanography. International Statistical Review 71 (2), 223–241.
Brusdal, K., Brankart, J., Halberstadt, G., Evensen, G., Brasseur, P., van Leeuwen, P., Dombrowsky, E., Verron, J., 2003. A demonstration of ensemble-based assimilation methods with a layered OGCM from the perspective of operational ocean forecasting systems. Journal of Marine Systems 40, 253–289.
Burchard, H., Bolding, K., Villarreal, M., 1999. GOTM — a general ocean turbulence model. Theory, applications and test cases. European Commission report EUR 18745.
Doney, S., Lima, I., Lindsay, K., Moore, J., Dutkiewicz, S., Friedrichs, M., Matear, R., 2001. Marine biogeochemical modeling: recent advances and future challenges. Oceanography 14 (4), 93–107.
Dowd, M., 2007. Bayesian statistical data assimilation for ecosystem models using Markov Chain Monte Carlo. Journal of Marine Systems 68 (3–4), 439–456.
Dowd, M., Meyer, R., 2003. A Bayesian approach to the ecosystem inverse problem. Ecological Modelling 168 (1–2), 39–55.
Evensen, G., 2003. The Ensemble Kalman Filter: theoretical formulation and practical implementation. Ocean Dynamics 53 (4), 343–367.
Evensen, G., 2006. Data Assimilation: The Ensemble Kalman Filter. Springer Verlag New York, Inc., Secaucus, NJ, USA.
Fennel, K., Boss, E., 2003. Subsurface maxima of phytoplankton and chlorophyll: steady-state solutions from a simple model. Limnology and Oceanography 48 (4), 1521–1534.
Fennel, K., Losch, M., Schröter, J., Wenzel, M., 2001. Testing a marine ecosystem model: sensitivity analysis and parameter optimization. Journal of Marine Systems 28 (1–2), 45–63.
Fennel, K., Wilkin, J., Levin, J., Moisan, J., O'Reilly, J., Haidvogel, D., 2006. Nitrogen cycling in the Middle Atlantic Bight: results from a three-dimensional model and implications for the North Atlantic nitrogen budget. Global Biogeochemical Cycles 20 (3). doi:10.1029/2005GB002456.
Fennel, K., Wilkin, J., Previdi, M., Najjar, R., 2008. Denitrification effects on air–sea CO_2 flux in the coastal ocean: simulations for the Northwest North Atlantic. Geophysical Research Letters 35, L24608. doi:10.1029/2008GL036147.
Friedrichs, M., 2001. A data assimilative marine ecosystem model of the central equatorial Pacific: numerical twin experiments. Journal of Marine Research 59, 859–894.
Friedrichs, M., Dusenberry, J., Anderson, L., Armstrong, R., Chai, F., Christian, J., Doney, S., Dunne, J., Fujii, A., Hood, R., et al., 2007. Assessment of skill and portability in regional marine biogeochemical models: role of multiple planktonic groups. Journal of Geophysical Research 112 (8). doi:10.1029/2006JC003852.
Garcia, H., Gordon, L., 1992. Oxygen solubility in seawater: better fitting equations. Limnology and Oceanography 37 (6), 1307–1312.
Geider, R., MacIntyre, H., Kana, T., 1996. A dynamic model of photoadaptation in phytoplankton. Limnology and Oceanography 41 (1), 1–15.
Geider, R., MacIntyre, H., Kana, T., 1997. Dynamic model of phytoplankton growth and acclimation: responses of the balanced growth rate and the chlorophyll a: carbon ratio to light, nutrient-limitation and temperature. Marine Ecology Progress Series 148 (1), 187–200.
Gneiting, T., Raftery, A., 2005. Weather forecasting with ensemble methods. Science 310 (5746), 248–249.
Gordon, N., Salmond, D., Smith, A., 1993. Novel approach to nonlinear/non-Gaussian Bayesian state estimation. Radar and Signal Processing, IEE Proceedings F 140 (2), 107–113.
Hofmann, E., Friedrichs, M., 2001. Biogeochemical data assimilation. Encyclopedia of Ocean Sciences 1, 302–308.
Ionides, E., Breto, C., King, A., 2006. Inference for nonlinear dynamical systems. Proceedings of the National Academy of Sciences 103 (49), 18438.
Kalnay, E., Kanamitsu, M., Kistler, R., Collins, W., Deaven, D., Gandin, L., Iredell, M., Saha, S., White, G., Woollen, J., et al., 1996. The NCEP/NCAR 40-Year Reanalysis Project. Bulletin of the American Meteorological Society 77 (3), 437–471.
Kantha, L., 2004. A general ecosystem model for applications to primary productivity and carbon cycle studies in the global oceans. Ocean Modelling 6 (3–4), 285–334.
Kishi, M., Kashiwai, M., Ware, D., Megrey, B., Eslinger, D., Werner, F., Noguchi-Aita, M., Azumaya, T., Fujii, M., Hashimoto, S., et al., 2007. NEMURO — a lower trophic level model for the North Pacific marine ecosystem. Ecological Modelling 202 (1–2), 12–25.
Kitagawa, G., 1996. Monte Carlo filter and smoother for non-Gaussian nonlinear state space models. Journal of Computational and Graphical Statistics 5 (1), 1–25.
Kitagawa, G., 1998. A self-organizing state-space model. Journal of the American Statistical Association 93 (443), 1203–1215.
Lawson, L., Hofmann, E., Spitz, Y., 1996. Time series sampling and data assimilation in a simple marine ecosystem model. Deep Sea Research Part II: Topical Studies in Oceanography 43 (2), 625–651.
Lek, S., 2007. Uncertainty in ecological models. Ecological Modelling 207 (1), 1–2.
Lenartz, F., Raick, C., Soetaert, K., Grégoire, M., 2007. Application of an Ensemble Kalman filter to a 1-D coupled hydrodynamic-ecosystem model of the Ligurian Sea. Journal of Marine Systems 68 (3–4), 327–348.
Losa, S., Kivman, G., Schröter, J., Wenzel, M., 2003. Sequential weak constraint parameter estimation in an ecosystem model. Journal of Marine Systems 43 (1–2), 31–49.
Mattern, J.P., 2008. Ensemble-based data assimilation for a physical–biological ocean model near Bermuda. Master's thesis, Universität zu Lübeck.
McGillicuddy, D., Robinson, A., Siegel, D., Jannasch, H., Johnson, R., Dickey, T., McNeil, J., Michaels, A., Knap, A., 1998. Influence of mesoscale eddies on new production in the Sargasso Sea. Nature 394, 263.
McGillicuddy Jr., D., Anderson, L., Doney, S., Maltrud, M., 2003. Eddy-driven sources and sinks of nutrients in the upper ocean: results from a 0.1 resolution model of the North Atlantic. Global Biogeochemical Cycles 17 (2). doi:10.1029/2002GB001987.
Moradkhani, H., Sorooshian, S., Gupta, H., Houser, P., 2005. Dual state–parameter estimation of hydrological models using ensemble Kalman filter. Advances in Water Resources 28 (2), 135–147.
Natvik, L., Evensen, G., 2003. Assimilation of ocean colour data into a biochemical model of the North Atlantic Part 1. Data assimilation experiments. Journal of Marine Systems 40, 127–153.
Ristic, B., Arulampalam, S., Gordon, N., 2004. Beyond the Kalman filter: particle filters for tracking applications. Artech House.
Rodi, W., 1987. Examples of calculation methods for flow and mixing in stratified fluids. Journal of Geophysical Research 92 (C5), 5305–5328.
Rothstein, L., Cullen, J., Abbott, M., Chassignet, E., Denman, K., Doney, S., Ducklow, H., Fennel, K., Follows, M., Haidvogel, D., Hoffman, E., Karl, D., Kindle, J., Lima, I., Maltrud, M., McClain, C., McGillicuddy, D., Olascoaga, J., Spitz, Y., Wiggert, J., Yoder, J., 2006. Modeling ocean ecosystems: the PARADIGM program. Oceanography 19 (1), 16–45.
Schartau, M., Oschlies, A., Willebrand, J., 2001. Parameter estimates of a zero-dimensional ecosystem model applying the adjoint method. Deep-Sea Research Part II 48 (8–9), 1769–1800.
Spitz, Y., Moisan, J., Abbott, M., 2001. Configuring an ecosystem model using data from the Bermuda Atlantic Time Series (BATS). Deep-Sea Research Part II 48 (8–9), 1733–1768.
Steinberg, D., Carlson, C., Bates, N., Johnson, R., Michaels, A., Knap, A., 2001. Overview of the US JGOFS Bermuda Atlantic Time-series Study (BATS): a decade-scale look at ocean biology and biogeochemistry. Deep-Sea Research Part II 48 (8–9), 1405–1447.
Turner, M., Walker, J., Oke, P., 2008. Ensemble member generation for sequential data assimilation. Remote Sensing of Environment 112 (4), 1421–1433.
Wanninkhof, R., 1992. Relationship between wind speed and gas exchange over the ocean. Journal of Geophysical Research 97 (C5), 7373–7382.
Wiggert, J., Murtugudde, R., Christian, J., 2006. Annual ecosystem variability in the tropical Indian Ocean: results of a coupled bio-physical ocean general circulation model. Deep-Sea Research Part II 53 (5–7), 644–676.